Anomaly of strain relaxation in thin ordered FePd layers

D. Halley,[1] Y. Samson,[1,*] A. Marty,[1] P. Bayle-Guillemaud,[1] C. Beigné,[1] B. Gilles,[2] and J. E. Mazille[3]
[1]*CEA Grenoble Département de Recherche Fondamentale sur la Matière Condensée, Service de Physique des Matériaux et Microstructure, 17 Avenue des Martyrs, 38054 Grenoble Cedex 9, France*
[2]*CNRS/LTPCM, ENSEEG, BP 75, 38402 Saint Martin d'Hères, France*
[3]*CEA Grenoble, CEREM/DEM/SPCM, 38054 Grenoble, France*
(Received 11 September 2001; revised manuscript received 23 January 2002; published 13 May 2002)

Strain relaxation processes have been investigated in chemically ordered FePd thin layers grown on Pd(001). Microtwins due to the pileup of $a/6\langle 211\rangle$ dislocations release most of the relaxation. A statistical analysis of scanning tunneling microscopy images provides a detailed understanding of the involved processes and indicates a linear dependence of the relaxation process upon the FePd thickness. Such an unusual behavior is confirmed by reflection high-energy electron diffraction and x-ray diffraction measurements. Through a modeling of the repulsion between the cores of the partial dislocations forming the microtwin, we put forward the mechanism explaining this discrepancy with the Matthews law.

DOI: 10.1103/PhysRevB.65.205408 PACS number(s): 68.37.−d, 68.55.−a

I. INTRODUCTION

Strain relaxation in thin epitaxial layers is a process of high technological importance. The mastery of the strain relaxation process is the key to the proper building of a large number of artificial structures, such as metallic or semiconductor multilayers, with a large range of applications using magnetic or optical properties. In case of a bidimensional growth, strain relaxation generally occurs through the introduction of misfit dislocations. Relaxation often proceeds only above a critical thickness, when the state of strain has allowed the accumulation of enough energy to afford the cost associated to the misfit dislocations. Next, the evolution of the strain is generally well described through Matthews law.[1] Basically, as the relaxation proceeds, the strain diminishes progressively with increasing layer thickness, thus providing less incentive (per volume unit) to create new dislocations. As a result, the formation rate of new dislocations slows down as the layer thickness increases. Though deviations from Matthews law are often encountered,[2] a progressive slowdown of the relaxation rate with increasing layer thickness is generally observed.

Here we describe the relaxation processes in equiatomic FePd alloys grown on Pd(001). These alloys exhibit an ordered AuCu (I) type structure ($L1_0$ phase) and have attracted a considerable interest due to their magnetic properties.[3] With proper growth conditions, the chemical ordering is uniaxial with the *c* axis perpendicular to the surface of the film (Fig. 1),[3–5] thereby leading to a large uniaxial (perpendicular magnetic anisotropy. Theoretical work[6] concerning the $L1_0$ phase in AuCu and AuNi suggests that this easy chemical ordering could be enhanced by the epitaxial stress due to the buffer. For FePd/Pd(001), the misfit amounts to about 1%. In this paper, we demonstrate that relaxation takes place mainly through the introduction of partial Shockley dislocations, namely, $1/6\langle 112\rangle$, as previously observed in similar systems.[6,7]

We observe a nearly constant relaxation rate process with increasing layer thickness. In order to establish and explain this result, we use the combination of various experimental techniques so as to provide a deep understanding of the relaxation processes. X-ray diffraction (XRD) and reflection high-energy electron diffraction (RHEED) measurements give access to the state of strain of the whole layer, but do not provide any information on the elementary mechanisms. Transmission electron microscope (TEM) observations demonstrate that microtwins, due to a pileup of misfit dislocations, contribute to the relaxation, but failed to provide a quantitative estimation of their contribution. We will show that a quantitative interpretation of scanning tunneling microscopy (STM) and atomic force microscopy (AFM) images of the surface of the FePd alloy leads to a deeper understanding of the relaxation mechanism. Indeed, it has been shown that defects like dislocations, buried in the film, can have a significant effect on the surface morphology.[8–10] As a result, STM or AFM images may contain information about the strain relaxation process and a few authors used these images to estimate the relaxation associated with isolated dislocations deforming the layer surface [EuTe films (Ref. 11), InAs (Ref. 12), and CaF_2 (Ref. 13)]. Models based on linear elasticity[8,14] allow a quantitative use of this information. Here surface modifications are induced by the microtwins and we establish a quantitative link between the surface morphology and the properties of the underlying defects. This provides the basis for a detailed interpretation of the relaxation data and allows us to explain the discrepancy with the Matthews law.

II. EXPERIMENTAL DATA

The samples were prepared by molecular beam epitaxy under ultrahigh vacuum (10^{-7} Pa) equipped with electron beam evaporators monitored by quartz microbalances. A Pd(001) surface was obtained by evaporating 60 nm of Pd on a 3-nm Cr seed layer grown on a MgO (001)-oriented substrate. Then the sample was annealed for 15 min at 700 K to smooth the Pd surface. Before the growth of the alloy layer, the Pd and Fe fluxes from the electron beam evaporators were first adjusted using the oscillations of the intensity of the specular spot in the RHEED pattern. Thereafter, both Fe

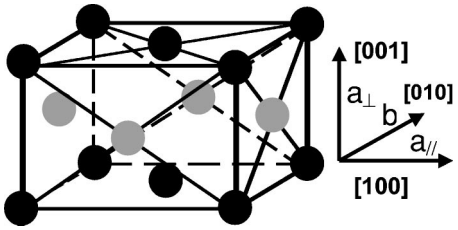

FIG. 1. Tetragonal $L1_0$ lattice: $a_{\perp,\mathrm{FePd}}=3.72$ Å, $a_{\parallel,\mathrm{FePd}}=3.85$ Å (Ref. 15). Black and gray circles correspond to the two different species Fe and Pd.

and Pd were simultaneously evaporated on the Pd(001) surface held at 620 K. Here Fe and Pd fluxes were both set to 0.16 monoatomic layer per second.

The RHEED diagram revealed the cube-on-cube relationship (001) [001] Pd/(001) [001] FePd. Finally, once back at room temperature, the sample was transferred into the adjacent chamber containing the scanning tunneling microscope [AFM-STM from Omicron GmbH, used under UHV conditions $(1-2\times10^{-8}$ Pa)]. For *ex situ* experiments, the alloy layer was next covered with a 2-nm Pd capping layer to prevent oxidation. A JEOL-4000EX microscope allowed the TEM observations, while AFM *ex situ* images were obtained using a Nanoscope IIIa from Digital Instruments. X-ray measurements were performed on a Microcontrol two-circle diffractometer using copper $K\alpha$ emission.

III. RESULTS

We first rely on XRD and RHEED to assess the state of strain of the FePd layer and to understand the nature of the relaxation defects.

A. XRD and RHEED observations

The lattice bulk parameter a of stoechiometric FePd is 0.380 nm in the case of a disordered alloy, but in the case of ordered structure, the fcc cell turns into fct [Fig. 1: $a_{\perp,\mathrm{FePd}}=3.72$ Å, $a_{\parallel,\mathrm{FePd}}=3.85$ Å (Ref. 15)]. The long-range order S of the alloy has been evaluated by x-ray diffraction. It is defined by $S=|n_{\mathrm{Fe}}-n_{\mathrm{Pd}}|$, where $n_{\mathrm{Fe\,(Pd)}}$ stands for the site occupancy of Fe atoms on the Fe (Pd) sublattice in the $L1_0$ phase. This parameter ranges from 0 for a completely disordered film to 1 for a perfectly ordered film. Here measurements yielded $S=0.8$.[3] Therefore, the lattice misfit ε between the Pd buffer and the ordered FePd was assessed at $\varepsilon=(a_{\mathrm{Pd}}-a_{\parallel,\mathrm{FePd}})/a_{\mathrm{Pd}}=1\%$.

The relaxation of the lattice parameter has been evaluated during the growth process by following the distance between 01 and 0-1 rods on the RHEED pattern. The relaxation curve (Fig. 2) is quite linear, which is not similar to the usual slow down of the rate of relaxation derived from widespread models.[1,2] The in-plane lattice parameters at the surface obtained from RHEED are consistent with x-rays results concerning the whole alloy layer. The XRD in-plane lattice parameters were obtained from the position of the {113} and {002} diffraction peaks.

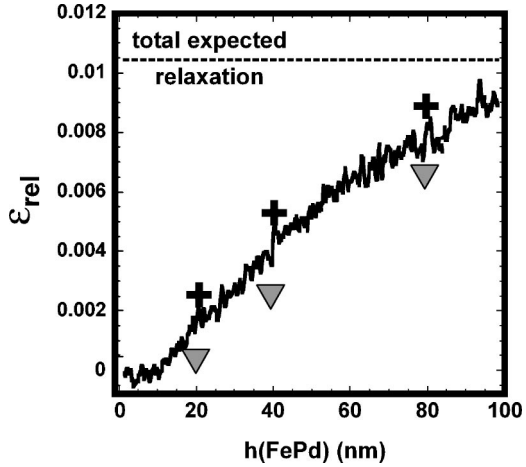

FIG. 2. Relaxation of the FePd layer ($\varepsilon_{\mathrm{rel}}=a_{\mathrm{Pd}}-a_{\parallel,\mathrm{FePd}}/a_{\mathrm{Pd}}$): $\varepsilon_{\mathrm{rel}}$ as a function of the thickness of the film [h(FePd)] from RHEED measurements performed during the growth process. The critical thickness is about 10 nm. (+) relaxation measured by XRD, (▼) mean relaxation values deduced when taking into account the contribution the microtwins from STM images. The dashed line corresponds to the value reached by $\varepsilon_{\mathrm{rel}}$ when the FePd layer is fully relaxed.

B. TEM observations

TEM has been used so as to identify the defects allowing the strain relaxation in the FePd/Pd(001) system. The [110] cross section of a 50-nm-thick FePd layer [Fig. 3(a)] shows a thin defect parallel to (111) planes, exhibiting a mirror symmetry compared to the rest of the crystal (relatively to {111} planes). This is a microtwin. The usual spacing observed between two such defects ranges from 50 to 200 nm. A large number of images has been realized, showing microtwins of quite constant thickness. Occasionally, two microtwins intersect, each other making an ''X,'' or stop on another one, forming a ''Y.'' Microtwins cross the whole FePd layer, most of them end at the interface, but a few cross the interface [Fig. 3(c)], coming down into the Pd layer.

Some lonely stacking faults and a few $1/2\langle011\rangle$ perfect dislocations were also observed.

C. Mechanism of the relaxation by microtwins

According to the literature, two kinds of dislocations are expected to accommodate the misfit in a fcc metallic thin film: $1/2\langle110\rangle$ perfect dislocations (with these, the Matthews equation[1] leads to a critical thickness of 8 nm) and $1/6\langle112\rangle$ partial Shockley dislocations. This latter mechanism has already been put forward:[4,7,16] $1/6\langle112\rangle$ partial dislocations nucleate at the surface of the alloy, glide along a {111} plane down to the interface with the Pd buffer. The glide of 1/6[112] dislocations along the (111) plane leads to a step at the surface of the film. These steps, being at the intersection of the (001) surface and of {111} planes, appear as $\langle110\rangle$ straight lines at the surface. The height of these discontinuities is equal to the perpendicular to the layer component of Burgers vector, i.e., $a_{\perp,\mathrm{FePd}}/3=0$, 124 nm. As these dislocations are partial, they leave a stacking fault on {111} gliding

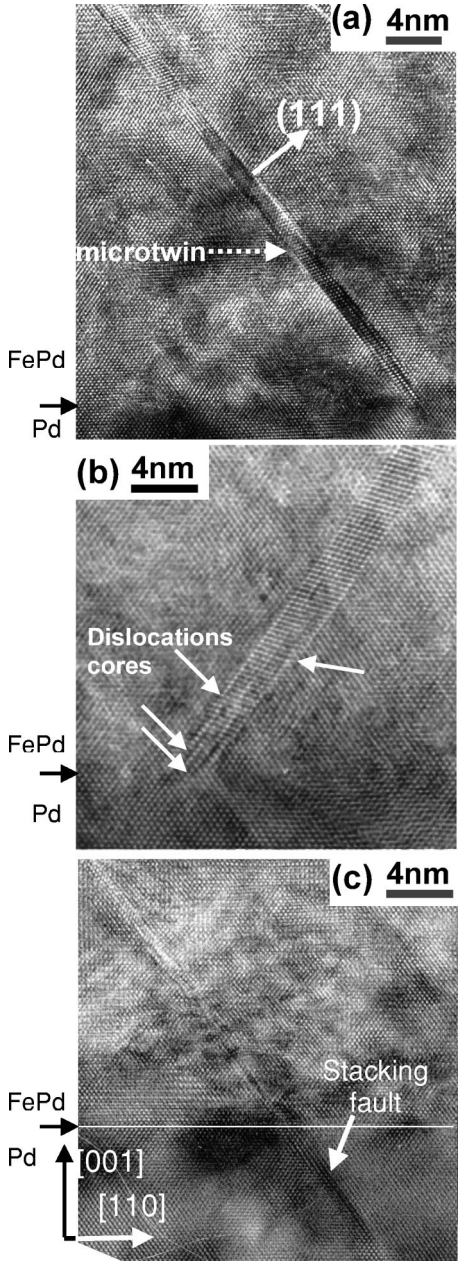

FIG. 3. TEM high-resolution images: sections of a 50-nm FePd layer seen along the [1-10] direction. Microtwins and dislocations cores are clearly observable [(a) and (b)]. A microtwin extending within the Pd buffer layer can be observed (c).

planes. Once one such partial dislocation has appeared, new partial dislocations are likely to glide along adjacent {111} planes. Indeed, this mechanism avoids the formation of additional faulted planes, which costs stacking fault energy. The volume contained between these two planes makes up a microtwin (see, for instance, in AuNi (Ref. 6), FePd (Ref. 4), Si/Ge multilayers (Ref. 7)]. N partial dislocations building a microtwin lead a $N^{*}a_{\perp,\mathrm{FePd}}/3$ step at the surface.

To illustrate these results, the elastic strain associated to such microtwins has been modeled under the assumption of isotropic elasticity using Head's equation[18] for buried dislocations parallel to the surface. In Fig. 4, the schematic representation shows both the step due to the emergence of the glide plane at the surface and the deformation field.

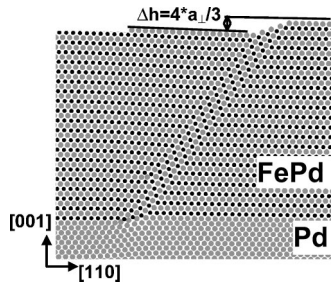

FIG. 4. Elastic modeling of the deformation around a microtwin, using Head's equations for buried dislocations $a/6\langle 112\rangle$ parallel to the surface. The FePd layer is 8 nm thick. Three out of the four partial dislocations ($N=4$) in the microtwin are located at the FePd/Pd interface. The step height (Δh) at the emergence of the microtwin corresponds to $N^{*}(a/3)$.

The favored relaxation by microtwins relatively to perfect dislocations seems to be linked with the ordering of the alloy: disordered films relax via perfect dislocations and do not exhibit microtwins. In fact, 1/2 [110] perfect dislocations cause antiphase boundaries in the $L1_0$ order and thus are not energetically favored. This point has to be further investigated.

D. STM observations: Qualitative analysis

As the link between the surface morphology and the underlying dislocations has been established, near-field images of the FePd surface bring now further information. At large FePd thickness [Figs. 5(b), 5(c), and 5(d)], the surface exhibits its remarkable features in addition to the growth steps already imaged on Fig. 5(b) [$h(\mathrm{FePd})=5$ nm]: straight lines are easily distinguishable along the two $\langle 110\rangle$ directions of the surface. These lines correspond to large steps up to about one nanometer [Fig. 5(d)]. They are the steps due to the emergence of microtwins at the surface. These steps end up on screw dislocations, which are the threading arms of the partial dislocations, coming up to the surface. Local analysis reveals that the height of the discontinuity step of a microtwin is not constant and is often larger in the middle of the line than close to its ends. It is likely that the threading arms of the partial dislocations are distributed along the microtwin, probably because of the repulsion between them. This leads to a pileup of dislocations of decreasing length. It thus explains the slightly variable step height of a microtwin: close to the ends the number of constitutive dislocations decreases. Other qualitative features are remarkable: the intersection of microtwins is a rare event except for thick layers. Often a microtwin stops on a perpendicular one [Figs. 5(b) and 5(c)], leading to the square pattern aspect of the surface. The surface density of microtwins appears quite similar for the different thickness of the alloy layer. However, the thicker film exhibits clearly more contrasted lines revealing higher steps (and then the pileup of more numerous dislocations).

It may be argued that perfect dislocations having a $1/2\langle 110\rangle$ Burgers vector, gliding on {111} planes would also

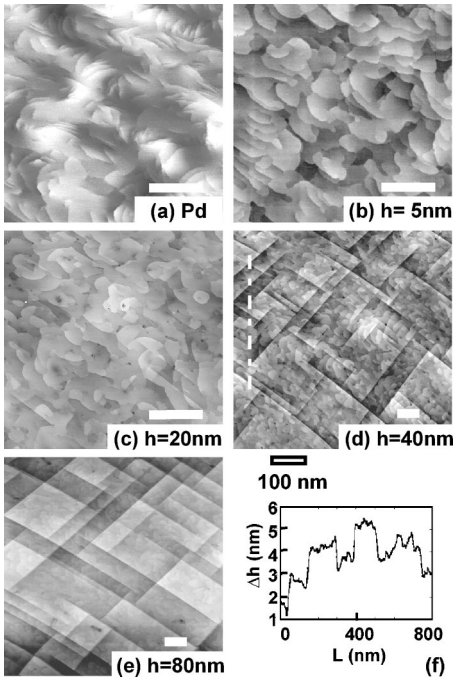

FIG. 5. 0.4-μm (a), (b), (c), 1-μm (d), (e) STM images of the surface of Pd(001) and of thin layers of ordered FePd alloy/Pd(001). Image (a) corresponds to the Pd(001) surface: atomic steps are visible, pinned on the emergence of screw dislocations. After the growth of 5 nm of alloy, the step density increases (b). In following images (c), (d), (e), the layer thickness exceeds the critical thickness, and straight lines, along 110 directions, correspond to the emergence of the microtwins. As the layer thickness increases, new partial dislocations pile up within the preexisting microtwins. This leads to higher steps (associated with the microtwins) formed at the surface, thereby increasing the contrast associated with the microtwins with respect to the contrast associated with the atomic steps. (f) Height profile along the line drawn on image (d).

cause a discontinuity on the surface. Such features would not be distinguished from a mere monoatomic step, ending on screw dislocations, and as any growth step, they would be bent because of the accumulation of adatoms during growth. Steps due to microtwins due to the pile up of N dislocations correspond to height $N^{*}a_{\perp,\mathrm{FePd}}/3$ steps, unlike $a_{\perp,\mathrm{FePd}}/2$ monoatomic steps. As a clear demonstration of the different nature of these two defects, it can be seen that some growth steps cross the lines associated with the emergence of to microtwins. These lines remain straight along $\langle 110\rangle$ directions during the growth process (see images of Fig. 5) as the steps associated with the microtwins (Fig. 4) do not lead to an accumulation of adatoms.

Due to uncorrected piezoelectric distortions, the upper and lower parts of the STM images are, respectively, reduced and dilated, and straight lines appear slightly bent.

IV. IMAGE ANALYSIS DISCUSSION

We now use STM images quantitatively so as to estimate the contribution of the microtwins to the relaxation process.

A. Image analysis process

A quantitative analysis was carried out on STM images shown in Fig. 5, using a Bild Kontron system dedicated to image analysis (consisting in dedicated processors and software). The aim of this analysis is to extract the contribution of the microtwins to the strain relaxation from the STM images. The heights of monoatomic ($a_{\perp,\mathrm{FePd}}/2$) and biatomic ($a_{\perp,\mathrm{FePd}}$) growth steps are close to the height of the step associated to small microtwins (exactly a for the pileup of three partial dislocations). Fortunately, microtwins are associated to straight and long lines along the $\langle 110\rangle$ directions, whereas the steps associated with the growth process are isotropic. To discriminate between mere growth steps and the emergence of microtwins, we used morphological filters consisting in matrix elements defining an element of line along $\langle 110\rangle$ directions. The filters are defined so as to preserve some tolerance with respect to a nonperfect alignment on the $\langle 110\rangle$ directions. Noticeably, portions of the growth steps running locally along these directions are not rejected, but they are easily scrapped thereafter as being too short to correspond to the emergence of a microtwin. This process leads to a binary image where lines of pixels corresponding to the emergence of a microtwin are outlined. Next, it is possible to measure the height Δh of the discontinuity at each point of these lines: the image of the local maxima (within a 5×5 pixel box) is first calculated, next, the image of the local minima, and finally, Δh corresponds to the difference between these two (maxima and minima) images, locally calculated at the position of the microtwins on the 521×512 pixels images.

This now enables us to calculate the number of partial dislocations in the microtwin at each point: $N=\Delta h/(a_{\perp,\mathrm{FePd}}/3)$. As expected, the histogram of the height Δh on a whole image (Fig. 6) evidences a discrete distribution of heights corresponding to multiples of $a_{\perp,\mathrm{FePd}}/3$.

These histograms yield quantitative data, such as the number of partial dislocations, the cumulated length of microtwins l in an image [Fig. 7(a)] and the mean number $\langle N\rangle$ of dislocations per microtwin on the image [Fig. 7(b)]. From

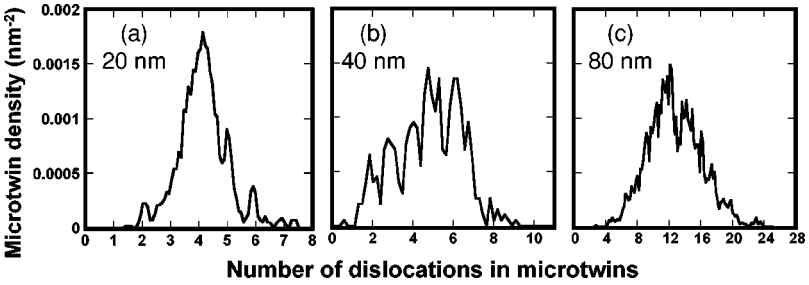

FIG. 6. Histograms of the step height associated with the emergence of the microtwins. Each one contains the data of the STM image of Fig. 5 of corresponding thickness. The plotted density is obtained as the length of the steps corresponding to the emergence of a microtwin, per unit of step height, per surface unit. The resulting density (nm^{-2}) is plotted as a function of the step height Δh, expressed as a number N of constitutive dislocations in microtwins ($N=\Delta h/a_{\perp,\mathrm{FePd}}/3$).

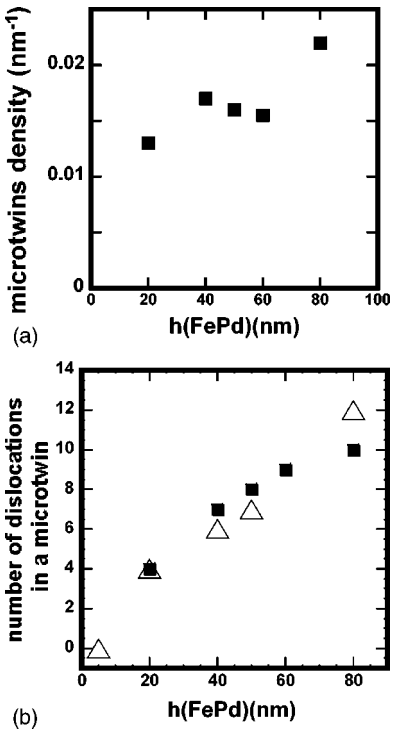

FIG. 7. (a) Total density of microtwins [length of microtwins per surface unit (nm^{-1})] as a function of the layer thickness h(FePd). Data extracted from STM images. (b) (△) Mean number of dislocations in microtwins as a function of the layer thickness h(FePd). Data extracted from STM images. (■) Predicted number of partial dislocations in a microtwin from elastic calculation.

the strain relaxed by one dislocation (equal to the component of Burgers vector parallel to the film, b_{para}) we were able to estimate the total relaxation due to microtwins within an image. This relaxation is given by $Nb_{\text{para}}l/(L^2)$, where L is the size of the image.

B. Amount of relaxation allowed by the microtwins

The measured relaxation is given in Table I for each ⟨110⟩ direction and also the ratio of the measured relaxation to the total expected relaxation. The relaxation via microtwins is comparable to the measured value obtained by RHEED or x rays. Moreover, for an 80-nm layer, the relaxation by microtwins is almost total in one direction. We can therefore conclude that the microtwins account for most of the relaxation process. They allow to relax 6% of the misfit in a 20-nm-thick layer and 90% in a 80-nm-thick FePd layer. This is consistent with the scarce observation of perfect $\frac{1}{2}\langle 110\rangle$ dislocations on TEM images: they seem to take on a negligible part of relaxation (such faults are not present on the TEM images we selected in this paper).

TABLE I. Evolution of the relaxation allowed by the microtwins as a percentage of the initial misfit. Data are extracted from STM images of Fig. 5 [except for the additional data at h(FePd) = 50 nm]. The data are first given for each ⟨110⟩ direction and next averaged over the two ⟨110⟩ directions.

FePd thickness (nm)	Relaxation along [110] (%)	Relaxation along [1-10] (%)	Average relaxation along the two directions (%)
20	0	6	3
40	22	29	25
50	12	28	20
80	33	90	62

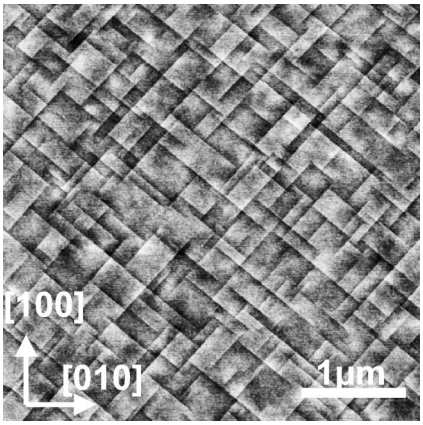

FIG. 8. 4-μm AFM image of the FePd surface. To allow observation in room conditions, the FePd layer was covered by a 1-nm Pd capping to protect it from oxidation. Steps due to microtwins are clearly observed.

A large difference of the calculated relaxation was observed along the two orthogonal equivalent ⟨110⟩ directions. This anisotropy may be explained by different assumptions: first, the MgO substrate may present a miscut along one of these directions (this miscut varies from a sample to the other but stays lower than 0.2°), promoting the development of defects in one direction. Such a long-range anisotropy in FePd should be detected by x-ray measurement of the lattice parameter, but the two in-plane lattice parameters proved to be equal, indicating that the relaxation is isotropic on large areas. In addition, the most relaxed direction is not always the same on a given sample, leaving aside the hypothesis of a long range miscut. Next, the size of the images ($1\ \mu$m $\times 1\ \mu$m) may be smaller than a characteristic length of this relaxation: a local fluctuation of the microtwins distribution would yield a local anisotropy. In order to check this last assumption, we performed wider images up to $8\ \mu$m $\times 8\ \mu$m. As this size exceeds the scanning range available in our UHV microscope, the measurement was performed by AFM at room conditions (Fig. 8). To avoid layer oxidation, a thin Pd capping (~1 nm) was first deposited. As it may prevent an accurate measurement of FePd surface heights, only surface densities of microtwins (l) along the two ⟨110⟩ directions are extracted from the images. Figure 9 plots the ratio of these two densities as a function of the image size: the anisotropy progressively decreases and nearly vanishes on an 8-μm image. This means that the anisotropy of the relaxation in a given image is only due to a statistical bias.

C. Density of microtwins

Beyond the average relaxation, STM images provide a deep understanding of the formation and coarsening of mi-

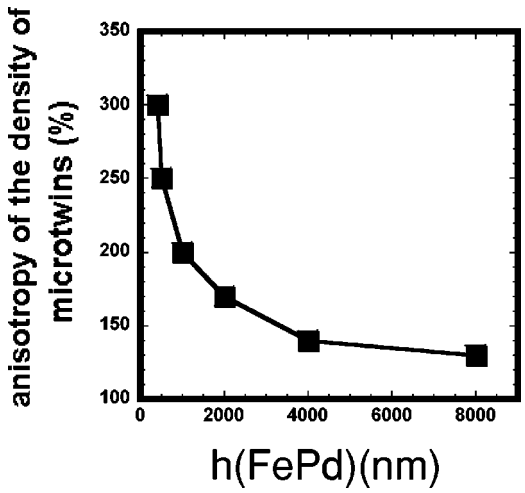

FIG. 9. Evolution of the ratio of the density of the two populations of microtwins (corresponding to the two ⟨110⟩ directions) as a function of the sampled area. The microtwin density (nm^{-1}) is obtained as the length of the steps corresponding to the emergence of a microtwin at the (001) surface, per surface unit.

crotwins: below the critical thickness for microtwin formation in FePd [Fig. 5(a)], there are no microtwins, because partial dislocations have not yet nucleated. In a 20-nm layer, microtwins are already present: the weak contrast observed on image 5(b) and the image analysis (Fig. 6) demonstrate that each microtwin contains only few partial dislocations. As the thickness of the layer increases, the microtwins get thicker, while their density increases only slowly [Fig. 7(a)]. This observation indicates that, after the nucleation of the first partial dislocations (above the critical thickness), the formation of new microtwins is a rare event. As a rule, the relaxation progresses via the pileup of additional dislocations in preexisting microtwins. This mechanism avoids the formation of new stacking faults.

A slightly higher density of microtwins is observed in thick films [Fig. 7(a)], but this does not prove so for the nucleation of new microtwins. Indeed, the number of microtwins is quite constant, but their length might vary. Most microtwins end up on perpendicular neighbors at low thickness (up to 40 nm), forming "T" intersections. The 20-nm-thick layer does not show any cross, while only 3 crosses and 51 "T" are observed for a 40-nm-thick layer. Conversely, microtwins intersect more easily in thick layers: there are 24 crosses$\cdot \mu m^{-2}$ and 40 "T"$\cdot \mu m^{-2}$ for the 80-nm-thick layer. This enables a lengthening of the preexisting microtwins, which were blocked by each other at lower thicknesses.

D. Size of the microtwins

The numerical analysis of the STM images demonstrates that the average number of dislocations per microtwin (N) is independent of the direction of the microtwin. Furthermore, this number clearly evolves with the FePd thickness: our data indicate an approximately linear dependence of N with h(FePd) [Fig. 7(b)].

As the surface density of the microtwins evolves slowly with h(FePd), the linear dependence of N upon h(FePd) leads to the linear dependence of the strain upon thickness. We will now explain the physical origin of this unusual behavior by using TEM observations to support an elastic modeling of the involved process.

V. TEM OBSERVATIONS OF THE DISLOCATIONS CORES AND ELASTIC MODELING

A. Experimental data

The linear dependence of the number of dislocations in microtwins can be explained by TEM observations of the dislocation cores. The number of (111) constitutive planes of a microtwin decreases towards the interface with Pd, leading to a wedge shape of the microtwin. Dislocation cores thus do not come down to the interface, but are spread out along the microtwin in its low part, close to the buffer layer [Fig. 3(b)]. Moreover, the spacing between each dislocation is not constant: dislocations appear to be more closely stacked very near to the Pd interface. This distribution of dislocations cores might allow one to minimize the repulsive energy between adjacent partial dislocations in the microtwin.

Interestingly, TEM observations [Fig. 3(c)] of microtwins getting into the Pd layer prove that some partial dislocations move down the interface, probably due to the force exerted by upper dislocations.[7] The large pileup of dislocations in the layer (more than ten dislocations) repels the lowest one into the palladium substrate, even if the driving force due to the misfit has vanished when the dislocation has entered the buffer layer. It proves that the repulsive energy between dislocations is large enough to influence the position of the cores inside the microtwins. The minimization of this energy might control the maximum number of dislocations in a microtwin, depending on the thickness of the layer. We then suggest that the repulsive interaction is the key to understanding the shape of the relaxation curve.

B. Elastic modeling

An elastic model is used to estimate the maximum number of dislocations in a microtwin: we consider N dislocations gliding on adjacent (111) planes, one dislocation being pined at the interface between Pd and FePd. In the following, three components of the energy of dislocations are in a balance: the self-energy of each dislocation, E_{self}: the interaction (repulsive) energy between all pairs of dislocations, $E_{\text{dis/dis}}$: and the interaction energy between the dislocations and stressed film of alloy, $E_{\text{dis/film}}$. These energy terms are calculated within the frame work of homogeneous and isotropic linear elasticity near a free surface (see the Appendix). We then calculate the different equilibrium of each dislocation, for a given number N of partials in a microtwin and for a given thickness h of the layer. We increase the number N of dislocations until one of the dislocations has no equilibrium position in the layer.

Figure 10 provides an instance of such a distribution for a 40-nm FePd layer. By varying h in the calculation, we obtain N as a function of h (Fig. 11). This estimation seems to be

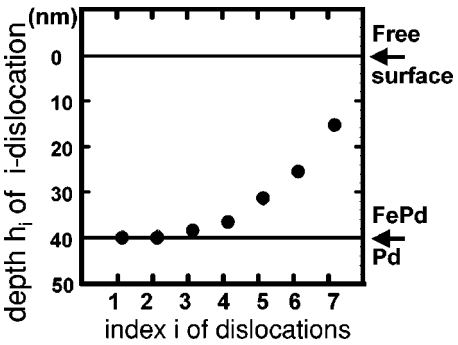

FIG. 10. In depth distribution of the dislocation cores within a 40-nm FePd layer. In the model, the first dislocation is pinned at the interface, while the position of the other ones result from a minimization of the total elastic energy. Here seven dislocations may be observed within the layer, the eighth one would not find a stable position within the available FePd layer thickness.

consistent with the observed size of microtwins by STM [Fig. 7(b)]. It suggests that the repulsion between dislocations inside the microtwins might be the controlling term in the pileup of new partial dislocations and then in the relaxation. Assuming a nearly constant density of microtwins and taking into account an almost linear dependence of $N(h)$, the relaxation appears to be linear as a function of the layer thickness. Noticeably, the asymmetric repartition of the dislocations lines, most of them being very close to the FePd/Pd interface, explains the good agreement between the surface strain measured by RHEED and the strain deduced from x-ray diffraction. Indeed, the small volume corresponding to the less relaxed part of the FePd layer, close to the interface, is limited enough to possibly induce an asymmetric widening of the x-ray diffraction peak, but no significant shift of the peak maximum, here measured to determine the lattice parameter.

Though some hypotheses are clearly untrue, this model should capture most of the physics. We have supposed that the deepest dislocation was pined at the interface between Pd and FePd, contrary to the observation of some dislocations that move down into the Pd layer. This could explain the discrepancy between the estimation of $N(h)$ obtained

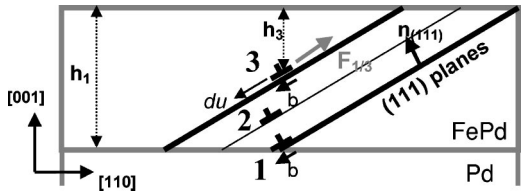

FIG. 11. Scheme of the repulsive forces between dislocations within a microtwin. The two black bold lines correspond to the stacking faults [(111) planes] delimiting the volume of the microtwin. h_i is the distance from the top surface of the *i*-dislocation core (of Burgers vector *b*). With the notation of the Appendix, *du* corresponds to the displacement of the considered dislocation and $F_{1/3}$ is the projection of the repulsive force exerted by dislocation 1 on dislocation 3. Here $n_{(111)}$ defines the direction perpendicular to the (111) plane. m^*d_{111} corresponds to the projection of the distance between the two considered dislocations along $n_{(111)}$, here $m=2$.

through the model and the experimental data at large FePd thicknesses. Indeed, this has been experimentally observed in TEM images of large microtwins resulting from the pileup of numerous dislocations (and hence at large thicknesses).

VI. CONCLUSION

Chemically ordered alloys attract a large interest due to their remarkable magnetic properties (Ref. 3 and references therein). The microtwins we described here explain some of these magnetic properties. Indeed, they provide a spontaneous square magnetic nanostructuration of the thin layer by being pinning sites for the magnetic domain walls.[16,17] This leads to the exceptionally large coercivity of thin layers of ordered alloys (FePd, FePt).

The investigation of strain relaxation processes in FePd thin layers grown on Pd(001) has been carried out thanks to RHEED, x-ray diffraction, and the quantitative use of surface images obtained through scanning probe microscopies. These techniques lead to a deep understanding of the relaxation mechanism. Indeed, TEM observations allow us to identify the defects associated with the relaxation process, here microtwins formed by the pileup of partial dislocations. Then STM images yield statistical information on the strain relaxation and prove that the microtwins take on most of the relaxation. Other systems could benefit from a similar use of STM images, provided that the elementary defects have been identified and that they cause an observable modification on the surface.

This unusual relaxation through the formation of microtwins causes a linear dependence of the strain upon the FePd thickness. This large deviation from usual expectations and from the Matthews law is linked to the very nature of the extended defects involved here. Indeed, as well, experimental data other than elastic modeling demonstrate that the repulsion between dislocation cores within the microtwin controls the introduction of new dislocations.

APPENDIX: REPARTITION OF THE DISLOCATION CORES INSIDE A MICROTWIN

We use a two-dimensional model. Hence dislocations are supposed to be infinite lines parallel to the surface, gliding on (111) planes, with 1/6[112] Burgers vector. The expressions for the elastic energy terms come from Head[18] and Dynna *et al.*[19] They take into account the effect of the free surface.

μ is the shear modulus of the elastic medium, ν is Poisson's ratio (here $\nu=0.3$), h the film thickness, b the magnitude of the Burgers vector of partial dislocations, β the angle between the Burgers vector and the dislocation line (here $\beta=\pi/2$), ϕ the angle between the misfit dislocation slip plane normal and the normal to the surface ($\phi=54°$), and $\mathbf{l}$ the dislocation line.

Repulsive energy between all dislocations, $E_{\text{dis/dis}}$

We first evaluate the general expression of the stress $[\sigma_{kl}]^{h_1}$ created by one dislocation within the whole film. The dislocation is located at a given depth h_1 under the surface

(Fig. 10). Next, applying the Peach-Köhler law projected on the (111) gliding plane, we evaluate the force $F_{1\to 2}$ exerted by a dislocation located at a depth h_1 on a second dislocation at h_2 gliding on a (111) plane. The two dislocations are separated by $(m_{12}-1)$ (111) planes (Fig. 10 provides a schematic definition of all parameters):

$$F_{1\to 2}=\sigma_{kl}^{h_1}(h_2,m_{12})b^k\cdot n^1.$$

Integrating $\vec{F}_{1\to 2}(h_1,h_2,m_{12})\cdot d\vec{u}$ with respect to h_2, along the (111) plane, from the surface to h_2, we obtain $E_{(h_1,m_{12})}(h_2)$, the interaction energy between the two dislocations.

For a distribution of N dislocations, the total repulsive energy can be written

$$E_{\text{disl/disl}}(h_1,\ldots,h_i,\ldots h_N)=\sum_{i<j} E_{(h_i,m_{ij})}(h_j).$$

Self-energy of each dislocation, E_{self}

Here

$$E_{\text{self}}^i=\mu b^2\frac{(1-\nu\cos^2\beta)}{4\pi(1-\nu)}\ln(2h_i/b)$$

$$=\mu b^2\frac{1}{4\pi(1-\nu)}\ln(2h_i/b)$$

for a dislocation i located at a distance h_i beneath the surface:

$$E_{\text{self}}^{\text{total}}(h_1,h_2,\ldots,h_N)=\sum_i E_{\text{self}}^i(h_i).$$

Interaction energy between dislocations and the stressed film of alloy, $E_{\text{dis/film}}$

$E_{\text{dis/film}}$ depends on the residual stress in the film. We estimate the remaining stress $f(h,0)$ at the surface of the film from experimental data: RHEED measurements performed during the growth process of the layer provide the surface lattice parameter as a function of the thickness of the layer h. At a depth h_i, for a layer of thickness h, $f(h,h_i)$ is the residual stress. Assuming that relaxation is only due to microtwins and that partial dislocations are spread inside microtwins, $f(h,h_i)$ is varying from $f(h,h)$ (=1%) at the interface with Pd to the measured value $f(h,0)$ at the surface of the alloy. Therefore each i dislocation is submitted to a residual stress $f_N(h,h_i)$ when located within a microtwin containing N dislocations:

$$f_N(h,h_i)=\frac{f_N(h,0)-f_N(h,h)}{N}i+f_N(h,h).$$

$f_N(h,0)$ is derived from RHEED measurements and $f_N(h,h)$ is taken independent of h and then amounts to 1%:

$$E_{\text{disl/film}}^i=-\frac{2\mu(1+\nu)}{(1-\nu)}f_N(h,i)h_i b\sin\beta\cos\varphi,$$

$$E_{\text{disl/film}}^{\text{total}}(h_1,h_2,\ldots,h_N)=\sum_i E_{\text{disl/film}}^i(h_i).$$

The total energy of the N dislocations of a microtwin can be written

$$E^{\text{total}}(h_1,h_2,\ldots,h_n)=E_{\text{disl/film}}^{\text{total}}+E_{\text{disl/film}}^{\text{total}}+E_{\text{self}}^{\text{total}}.$$

We set $h_1=h$ (the lowest dislocation is pined at the interface between Pd and FePd). This does not take into account the fact that the lowest dislocation is sometimes repelled within the Pd buffer [see Fig. 3(c)].

Minimizing E^{total} relatively to every h_i, for a given thickness h of the film and a given number N of dislocations, yields the different equilibrium position h_i of the dislocations. N is increased until we find $h_N=0$, which means that the latest dislocation would be repelled to the surface by the other dislocations and cannot find an equilibrium position within the alloy layer. We therefore can estimate $N(h)$.

*Corresponding author. FAX: (33) 4 38 78 50 97. Electronic address: ysamson@cea.fr

[1] J. W. Matthews and A. E. Blakeslee, J. Cryst. Growth **27**, 118 (1974).
[2] B. A. Fox and W. A. Jesser, J. Appl. Phys. **68**, 2801 (1990).
[3] V. Gehanno, A. Marty, B. Gilles, and Y. Samson, Phys. Rev. B **55**, 12 552 (1997).
[4] V. Gehanno, Ph.D thesis, Institut National Polytechnique de Grenoble, 1996.
[5] D. Halley, Y. Samson, A. Marty, C. Beigné, and B. Gilles, Surf. Sci. **481**, 25 (2001).
[6] M. Dynna, A. Marty, B. Gilles, and G. Patrat, Acta Mater. **45**, 257 (1997).
[7] W. Wegscheider, K. Eberl, G. Abstreiter, H. Cerva, and H. Oppolzer, Appl. Phys. Lett. **57**, 1496 (1990).
[8] G. Springholz and G. Bauer, Mater. Sci. Eng., B **37**, 96 (1996).
[9] F. Cléton, B. Sieber, A. Lefebvre, A. Bensaada, R. Masut, J. M. Bonard, J. D. Ganière, and M. Ambri, J. Appl. Phys. **80**, 827 (1996).
[10] P. Sutter and M. G. Lagally, Phys. Rev. Lett. **82**, 1490 (1999).
[11] N. Frank, G. Springholz, and G. Bauer, Phys. Rev. Lett. **73**, 2236 (1994).
[12] J. G. Belk, D. W. Pashley, B. A. Joyce, and T. S. Jones, J. Vac. Sci. Technol. A **15**, 915 (1997).
[13] H. Zog, C. Maissen, S. Blunier, S. Teodoropol, R. M. Overney, T. Richmond, and H. Haefke, J. Cryst. Growth **127**, 668 (1993).
[14] G. Springholz, G. Bauer, and V. Holy, Surf. Sci. **365**, 453 (1996).
[15] W. B. Pearson, *Handbook of Lattice Spacings and Structures of Metals*, revised ed., edited by G. V. Raynor (Pergamon, New York, 1964).
[16] M. H. Hong, K. Hono, and M. Watanabe, J. Appl. Phys. **84**, 4403 (1998).
[17] J. P. Attané, Y. Samson, A. Marty, and D. Halley, Appl. Phys. Lett. **79**, 794 (2001).
[18] A. K. Head, Proc. Phys. Soc. London, Sect. B **66**, 793 (1953).
[19] M. Dynna, T. Okada, and G. C. Weatherly, Acta Metall. Mater. **42**, 1661 (1994).